How to cite: *Angew. Chem. Int. Ed.* **2025**, *G4*, e202418707
doi.org/10.1002/anie.202418707

Nanozymes | Very Important Paper

sp Carbon Disrupting Axial Symmetry of Local Electric Field for Biomimetic Construction of Three-Dimensional Geometric and Electronic Structure in Nanozyme for Sensing and Microplastic Degradation

Yujian Sun, Chenguang Wang, Haoxin Li, Kai Wang, Qiang Bai, Guoli Zhang, Shuishui Feng, Lina Wang,* Zhiling Zhu,* and Ning Sui**

Abstract: The catalytic efficiency of natural enzymes depends on the precise electronic interactions between active centers and cofactors within a three-dimensional (3D) structure. Single-atom nanozymes (SAzymes) attempt to mimic this structure by modifying metal active sites with molecular ligands. However, SAzymes struggle to match the catalytic efficiency of natural enzymes due to constraints in active site proximity, quantity, and the inability to simulate electron transfer processes driven by internal electronic structures of natural enzymes. This study introduces a universal spatial engineering strategy in which molecular ligands are replaced with graphdiyne (GDY) to induce d-π orbital hybridization with copper nanoparticles (Cu NPs), leading to an asymmetric electron-rich distribution along the longitudinal axis that mimics the local electric field of natural laccase. Moreover, multiple sp bonds within GDY scaffold effectively anchor Cu NPs, facilitating the construction of 3D geometric structure similar to that of natural laccase. An enzymatic activity of 82.53 Umg^{-1} is achieved, 4.72 times higher than that of natural laccase. By reconstructing both 3D structures and local electric fields of natural enzymes through d-π orbital hybridization, this approach enhances electron interactions between cofactors, active centers, and substrates, and offers a versatile framework for biomimetic design of nanozymes.

Introduction

In nature, enzymatic reactions depend on the three-dimensional (3D) structure formed by the interactions between active centers and cofactors.[1–3] This structure effectively captures substrates and coordinates electron distribution between substrates and active centers, facilitating efficient catalysis.[4–6] To mimic this 3D structure in artificial enzymes, two primary strategies are currently employed. The first strategy involves introducing molecular ligands along the axial direction of single-atom active centers in single-atom nanozymes (SAzymes). By disrupting the axial symmetry of electron distribution, this method alters substrate adsorption and enhances enzyme-like activity.[7,8] For instance, Qu et al. improved peroxidase (POD)-like activity by employing a dimensionality engineering strategy.[9] They transformed conventional 2D FeN_4C centers into 3D structures by integrating oxidized sulfur functionalities onto the carbon plane. In this catalytic process, the single Fe site acts as the catalytic site, while the oxidized sulfur functions as the binding site, resulting in a 6.8-fold increase in activity compared to conventional FeN_4C SAzymes. However, this approach is constrained by the adaptability of atomic centers and axial ligands,[10] where the effectiveness of SAzymes depends on ligand type, binding capacity, molecular configuration, and chemical properties of ligands.[11,12]

Another strategy to enhance enzyme-like activity involves stacking bimetallic active centers axially to create vertically aligned dual-atom nanozymes that mimic asymmetric electron distributions.[13] For example, Na et al. developed a hollow Mo—Pt dual-atom nanozyme (H-MoN_5@PtN_4/C) using a two-tier template capture method that disrupts the usual d-π conjugation,[14] splits the Mo 4d orbitals, and causes the rearrangement of spin electrons. This designed nanozyme exhibits both catalase (CAT)-like and enhanced oxidase (OXD)-like activities. Similarly, Wong et al. engineered a vertically stacked Fe–Cu dual-atom nanozyme by assembling negatively charged iron phthalocyanine onto a positively charged copper-based 2D structure via strong non-covalent interactions and electrostatic forces.[15] This strategy mimics the electron coupling

[*] Y. Sun, C. Wang, H. Li, K. Wang, Prof. Dr. Q. Bai, S. Feng, Prof. Dr. Z. Zhu, Dr. N. Sui
College of Materials Science and Engineering, Qingdao University of Science and Technology, 53 Zhengzhou Road, Qingdao, Shandong 266042, China
E-mail: baiqiang@qust.edu.cn
zlzhu@qust.edu.cn
suining@qust.edu.cn
G. Zhang, Prof. Dr. L. Wang
College of Environment and Safety Engineering, Qingdao University of Science and Technology, 53 Zhengzhou Road, Qingdao, Shandong 266042, China
E-mail: linawang@qust.edu.cn
Prof. Dr. Z. Zhu, Dr. N. Sui
Key Laboratory of Optic-electric Sensing and Analytical Chemistry for Life Science, MOE; Shandong Key Laboratory of Biochemical Analysis, Qingdao University of Science and Technology, 53 Zhengzhou Road, Qingdao, Shandong 266042, China

and synergy observed in natural cytochrome c oxidase during oxygen activation. While these designs significantly boost enzyme-like activity, they require meticulous design and tedious synthesis to construct complex catalytic environments.[16,17] These methods primarily focus on precisely controlling the axial coordination between bimetallic centers and their atomic density to mimic the geometry of axial ligand,[18,19] which frequently overlooks the wider range of electron transfer mechanisms between cofactors and active centers.[20–24] This highlights the need for a more universal spatial engineering strategy that surpasses the limitations of atomic active centers and molecular-level ligands, allowing for simpler synthesis methods and the use of more general coordination materials.

Natural enzymes possess local electric field (LEF), generated by the asymmetric distribution of electrons across different domains, to promote electron transfer during catalysis.[25,26] For example, in cytochrome P450 reductase, the double protonation of a specific histidine residue during oxygen activation creates LEF that enhances rapid electron transfer and accelerates the enzymatic reaction,[27] This intrinsic electric field is crucial for regulating enzyme activity and offers valuable insights for designing biomimetic nanozymes.[28–30] Therefore, mimicking the asymmetric LEF to facilitate efficient electron transfer between active centers, cofactors, and substrates emerges as a promising strategy for biomimetic design of nanozymes.

In this study, the cofactor of natural enzymes was mimicked using a novel two-dimensional periodic material, graphdiyne (GDY),[31–33] which incorporates both sp and sp^2 hybridized carbon atoms.[34,35] On one hand, the high surface area and layered structure of GDY enable ligand selection beyond molecular constraints,[36,37] achieving a biomimetic construction of the 3D geometric structure of natural enzymes. On the other hand, the d-π interaction between the GDY scaffold and metal nanoparticles eliminates the need for axial stacking in bimetallic atoms, simplifying the demands on the active center and synthesis in construction of LEF of natural enzymes.[38,39] The presence of multiple sp bonds within the GDY scaffold further enhances the local asymmetric electric field and simulates a broader range of LEF,[40] effectively simulating the electronic behavior of natural enzymes by accelerating electron transfer between the substrate and the nanozyme. On this basis, a 3D nanozyme was developed by anchoring ultrasmall copper nanoparticles (Cu NPs) within a sandwich-like structure of GDY and graphene (G), designated as G/Cu/GDY. Both theoretical calculations and experimental analyses confirmed that GDY improves the adsorption of oxygen and substrates.[41] The synergistic effects of sp-hybridized carbon led to d-p hybridization between the p orbitals of oxygen atoms and the enhanced d orbitals of copper atoms.[42,43] This interaction allows free electrons on the copper surface to quickly occupy the antibonding orbitals of oxygen, lowering the energy barrier and accelerating the four-electron reduction of oxygen to water. By mimicking both the geometric and electronic structures of natural enzymes, this 3D nanozyme demonstrates a laccase-like activity of 82.53 Umg^{-1}, which is 4.72 times higher than that of natural laccase. This high catalytic activity enhances the sensitivity and selectivity of pollutant detection in real water systems and enables efficient degradation of microplastic pollutants.[44,45] Moreover, the substantial improvement in nanozyme stability allow for excellent recyclability in detection applications under complex environmental conditions and great potential for high-temperature degradation of microplastic pollutants.

Results and Discussion

Synthesis and Characterization of G/Cu/GDY Nanozyme

Figure 1a illustrates the synthesis process of the G/Cu/GDY nanozyme. Initially, copper ions were reduced in situ at 160 °C using ethylene glycol, which serves as both a stabilizing and reducing agent. This step produces a graphene/copper (G/Cu) composite. Subsequently, a thin layer of GDY was synthesized in situ on the prepared G/Cu composite using a hexaynylbenzene (HEB) monomer, resulting in the formation of a 3D sandwich structure composed of graphene, GDY, and Cu NPs, referred to as G/Cu/GDY.

The morphology of the G/Cu/GDY and G/Cu composites was characterized using transmission electron microscopy (TEM), which reveals a uniform distribution of Cu NPs ranging from 3 nm to 5 nm in size (Figure 1b; Figure S1a, b). TEM images at various magnifications (Figure 1c) confirm the successful coating of GDY on the surface of the Cu NPs. High-resolution transmission electron microscopy (HRTEM) shows a lattice spacing of 0.21 nm for Cu NPs in G/Cu/GDY (Figure 1d). In contrast, the lattice spacing for Cu NPs in G/Cu is 0.20 nm (Figure S1c), indicating that the GDY coating does not alter the crystallographic structure of Cu NPs. Energy-dispersive X-ray spectroscopy (EDS) demonstrates that the G/Cu/GDY nanozyme is primarily composed of uniformly distributed carbon and copper elements (Figure 1e; Figure S1d). Scanning electron microscopy (SEM) shows that both graphene and GDY in the G/Cu/GDY nanozyme form thin, layered sheets that effectively encapsulate the Cu NPs (Figure S2).

The X-ray diffraction (XRD) patterns (Figure 1f) for both G/Cu and G/Cu/GDY display characteristic copper peaks at 43.30°. These peaks exhibit reduced intensity and noticeable broadening, due to the small size of Cu NPs.[46] When compared to the standard powder diffraction file (PDF) #04–0836, the peak at 43.30° corresponds to the (111) crystal plane. This observation aligns with the lattice spacing measured in HRTEM. Additionally, a peak at 26.38° is attributed to the characteristic diffraction of carbon. Distinct diffraction peaks for graphene and GDY are not evident, due to their thin-layer structure and low crystallinity. The Raman spectra of G/Cu/GDY and G/Cu (Figure 1g) display peaks at 1339 cm^{-1} and 1579 cm^{-1}, corresponding to the D and G bands, respectively. In addition, the G/Cu/GDY spectrum shows a peak at 2109 cm^{-1}, attributed to the C≡C bond vibration in GDY,[47] validating the presence of GDY and the structures of graphene and GDY remain unaltered by incorporation of Cu NPs. Particle size distribution

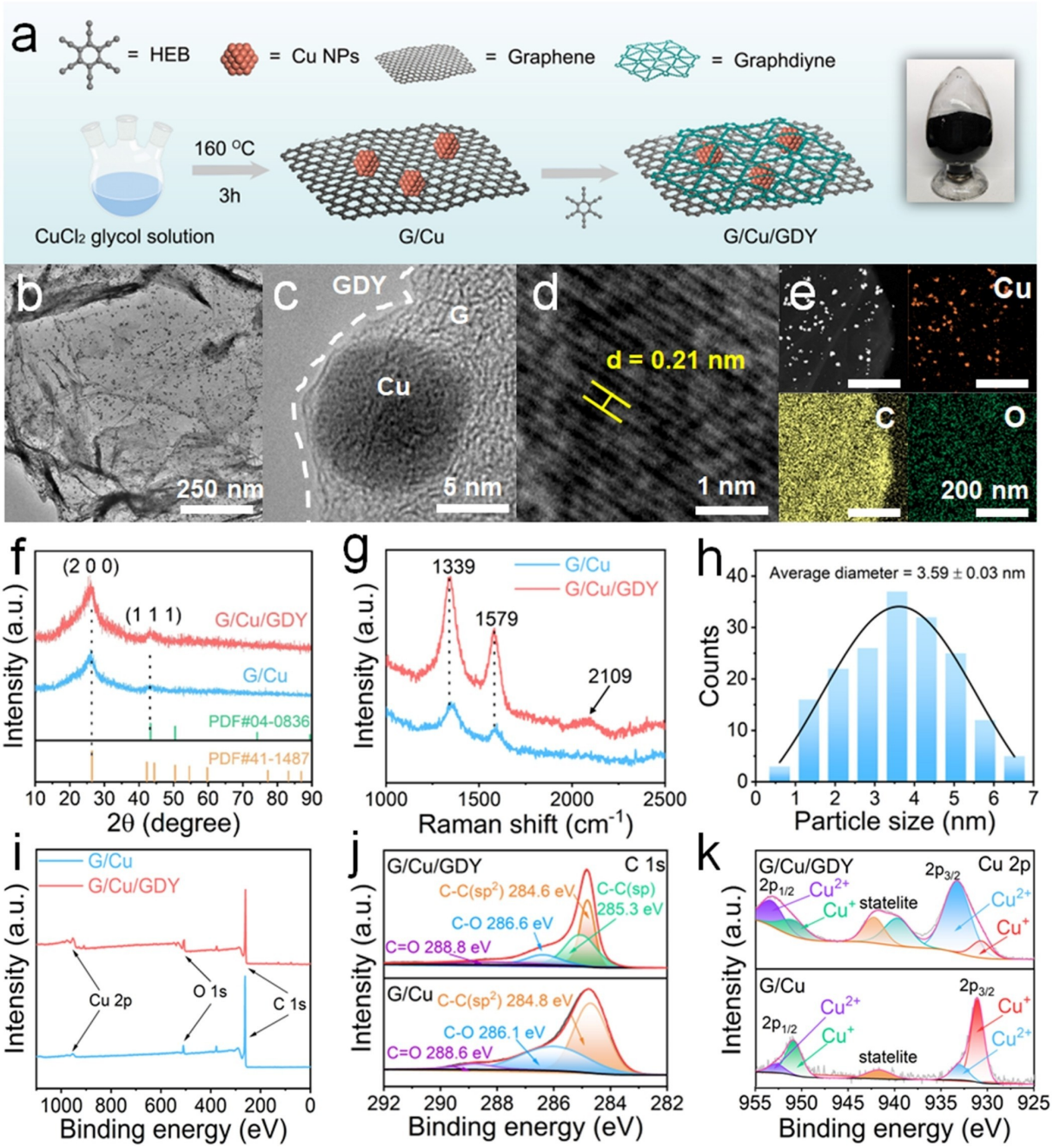

Figure 1. Synthesis and characterization of G/Cu/GDY nanozyme. (a) Schematic illustration of the synthesis of G/Cu/GDY and the image of final product. (b) Transmission electron microscopy (TEM) image of G/Cu/GDY. (c) High-magnification TEM image of G/Cu/GDY. (d) High-resolution TEM image (HRTEM) of G/Cu/GDY. (e) Energy-dispersive X-ray spectroscopy (EDS) elemental spectrum of G/Cu/GDY. (f) X-ray diffraction (XRD) patterns of G/Cu/GDY and G/Cu. (g) Raman spectra of G/Cu/GDY and G/Cu. (h) Particle size distribution of G/Cu/GDY. (i) X-ray photoelectron spectroscopy (XPS) survey spectra of G/Cu/GDY and G/Cu. (j) XPS C 1s spectra of G/Cu/GDY and G/Cu. (k) XPS Cu 2p spectra of G/Cu/GDY and G/Cu.

analysis using Gaussian fitting reveals that the Cu NPs in G/Cu/GDY have an average diameter of 3.59±0.03 nm (Figure 1h).

X-ray photoelectron spectroscopy (XPS) further confirms the presence of carbon and copper in both G/Cu/GDY and G/Cu (Figure 1i). The C 1s XPS spectrum of G/Cu/GDY (Figure 1j) exhibits peaks at 284.6 eV and 285.3 eV, corresponding to C–C (sp^2) and C–C (sp) bonds, respectively. Notably, the C–C (sp) peak in G/Cu/GDY is right shifted by 0.2eV compared to GDY alone. Meanwhile, the Cu 2p XPS spectrum for G/Cu/GDY shows a left shift by 0.4 eV relative to G/Cu (Figure 1k). The binding energy shift indicates electron transfer between Cu NPs and GDY, probably resulting from the interaction between the GDY

shell and the surface electrons of the Cu NPs, where electrons transfer from the Cu NPs to the GDY shell. Moreover, this electron migration increases the electron density on the GDY surface, reducing its binding energy, while the Cu NPs experience an increase in binding energy due to electron depletion.[48] The XPS results confirm a strong interaction between GDY and Cu NPs, with significant electron transfer through diacetylene bonds, thereby altering the surface electronic distribution of the Cu NPs.

Exploration of LEF in G/Cu/GDY Nanozyme

Figure 2a shows the microscopic structure of the synthesized G/Cu/GDY nanozyme. Coordination bonds formed among graphene, GDY, and Cu NPs facilitate the modulation of surface electrons along the axial direction of the Cu NPs. This interaction disrupts the axial symmetry of the Cu NPs, resulting in a high-energy active surface that mimics the role of cofactors in natural laccases. Differential charge density calculations comparing G/Cu/GDY with G/Cu reveal a charge transfer of 0.5 eV to the surface of G/Cu/GDY (Figure 2b, c), confirming the strong electron-accepting interaction between GDY and Cu NPs. In addition, electronic localization function (ELF) analysis (Figure S3) shows that the intensity around the Cu–C bond is below 0.15, indicating an ionic interaction within Cu–C bond coupling by a relatively strong electron exchange. All these results highlight the significant role of GDY in enhancing the electron modulation capabilities of Cu NPs, thereby contributing to the overall efficiency of nanozymes in mimicking laccase activity.[49,50]

To further evaluate the influence of GDY on the surface electronic properties of Cu NPs, the zero-field cooled magnetic susceptibility of both G/Cu/GDY and G/Cu across a range of temperatures was measured. The effective magnetic moments were found to be 3.96 μeff for G/Cu/GDY and 2.25 μeff for G/Cu (Figure 2d, e). For G/Cu, the

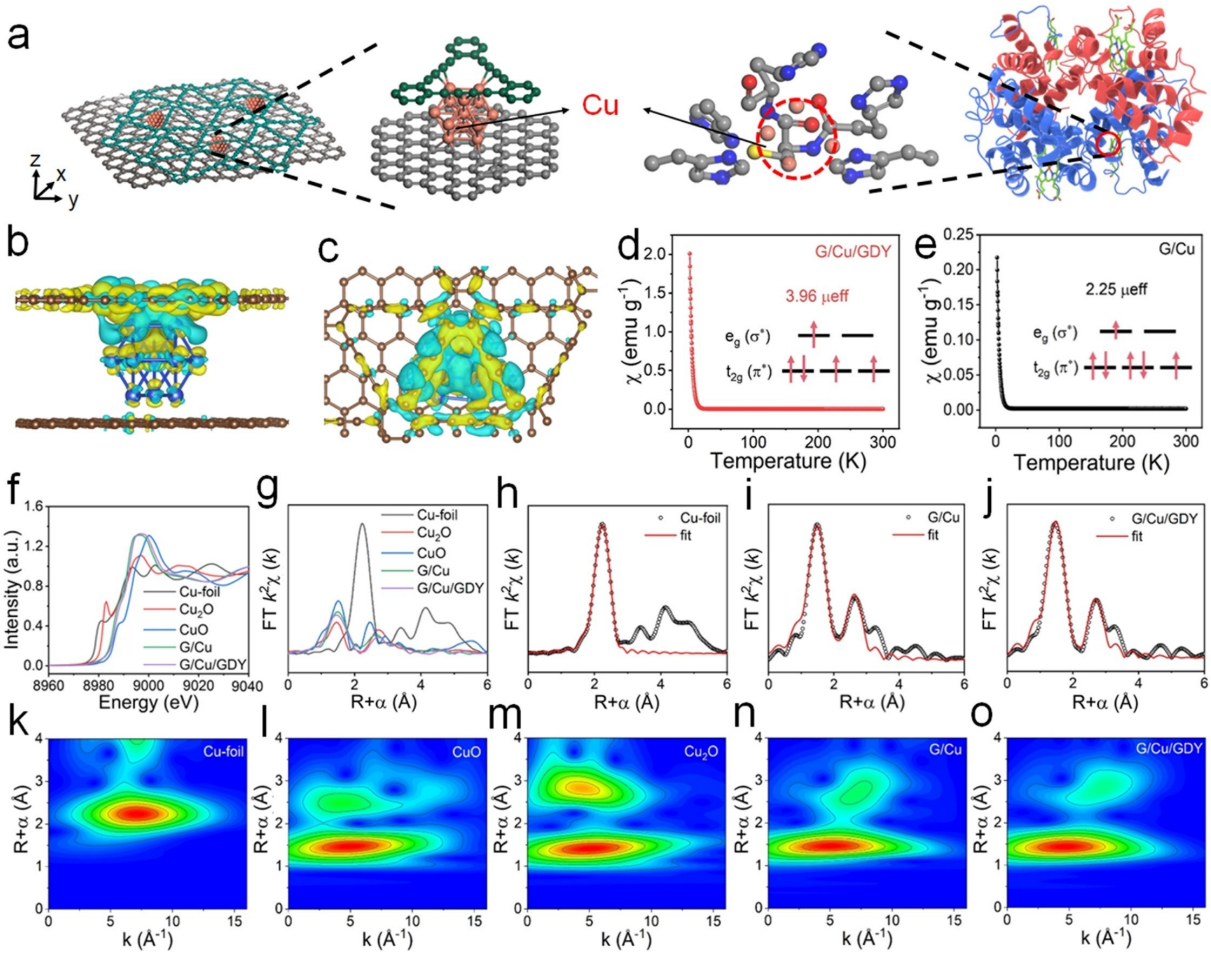

Figure 2. Construction of LEF in G/Cu/GDY nanozyme. (a) Schematic diagram of the structure of the G/Cu/GDY nanozyme. (b, c) Differential charge density maps of G/Cu/GDY from different perspectives. (d, e) Magnetization versus temperature curves for (d)G/Cu/GDY and (e)G/Cu, fitted according to Curie–Weiss law. Insets show the electron occupancy of t_{2g} and e_g anti-bonding orbitals. (f) X-ray absorption near-edge structure (XANES) spectra for G/Cu/GDY, G/Cu, CuO, Cu_2O, and Cu foil. (g) Fourier-transform extended X-ray absorption fine structure (FT-EXAFS) spectra for G/Cu/GDY, G/Cu, CuO, Cu_2O, and Cu foil. (h–j) EXAFS quantitative curve fitting analysis for (h) Cu foil, (i) G/Cu, and (j) G/Cu/GDY. (k–o) Wavelet-transform EXAFS (WT-EXAFS) contour plots for (k) Cu foil, (l) CuO, (m) Cu_2O, (n) G/Cu, and (o) G/Cu/GDY.

number of unpaired electrons was calculated to be 1.46, implying that Cu NPs are in a low-spin state. The presence of empty e_g orbitals and the unoccupied σ* anti-bonding orbitals suggests a tendency for Cu NPs to form stable structures with O_2.[48] In contrast, G/Cu/GDY exhibits 3.08 unpaired electrons, with the singly occupied e_g orbitals contributing to its significantly enhanced catalytic activity. This observation demonstrates the substantial impact of GDY on altering the surface electronic properties of Cu NPs, which in turn enhances their catalytic efficiency.

X-ray absorption near edge structure (XANES) spectroscopy confirmed that the coordination environment of Cu NPs underwent significant changes (Figure 2f). In the G/Cu and G/Cu/GDY composite structures, the interaction between Cu NPs and G/GDY altered the electronic configuration of the copper surface, making its oxidation state closer to Cu^{2+}. However, in the G/Cu/GDY nanozyme, due to the combined effect of graphene and GDY, the electronic coordination of Cu NPs changed more significantly, making its K-edge spectrum closer to Cu^{2+}, indicating that more electron transfer occurred between Cu NPs and GDY in the G/Cu/GDY structure.

Analysis of the Fourier-transform k^2-weighted extended X-ray absorption fine structure (FT-EXAFS) spectra and Cu–K edge EXAFS fitting data revealed a distinct main peak at 1.47 Å (without phase correction) in G/Cu/GDY and G/Cu (Figure 2g). In the wavelet transform (WT) profile in k-space, the maximum value at 6.2 $Å^{-1}$ was assigned to Cu–Cu and Cu–C bonds (Figure S4). The projection of the entire spectrum along the vertical axis is consistent with conventional Fourier transform curves. By comparing the WT images of Cu-foil, CuO, Cu_2O, G/Cu/GDY, and G/Cu, strong WT signals corresponding to the Cu–C shell were observed at the corresponding R-space positions for both G/Cu/GDY and G/Cu. A detailed comparison of peak intensities showed that the intensity of G/Cu was 1.16, which is higher than that of G/Cu/GDY (1.02), indicating that the introduction of GDY not only affected the Cu–C bond length but also changed the surrounding coordination environment of Cu. Both FT-EXAFS and WT-EXAFS results confirm that the Cu NPs in G/Cu/GDY and G/Cu are closer to the oxidation state of Cu.

Further analysis of the Cu–K edge EXAFS fitting data shows that the first coordination shell in both G/Cu/GDY and G/Cu structures corresponds to Cu–C bonds (Figure 2h–j). Additionally, no Cu–Cu bonds matching standard copper foil were found in the G/Cu/GDY and G/Cu structures. However, in G/Cu/GDY, a Cu—Cu signal was observed at 2.70 Å, similar to the signals in Cu_2O and CuO samples. Notably, this Cu–Cu signal was also observed in the G/Cu structure, but with a slightly shorter Cu–Cu bond length (2.64 Å) compared to G/Cu/GDY. This may be due to the attraction of GDY to copper electrons, causing delocalization of the Cu atoms and altering the bond length. This hypothesis is supported by the EXAFS fitting data (Table S1). We observed a significant difference in coordination numbers between G/Cu/GDY and G/Cu. Compared to G/Cu, the surface coordination number in the G/Cu/GDY structure decreased by approximately 0.5, while the coordination number of Cu–Cu bonds in the center did not change significantly. This is likely due to the combined interaction of graphene and GDY on Cu NPs along the axial direction, leading to more electron transfer from the nanoparticle surface to the C atoms, making the surface copper more similar to its oxidized state and reducing its coordination number. XANES analysis of the C element in G/Cu/GDY and G/Cu reveals the presence of the unique alkyne π excitation state of GDY at 286.1 eV, which is absent in the G/Cu structure, confirming the existence of GDY in the system (Figure S5). Additionally, in the G/Cu/GDY structure, the sp^2–C peak at 285.7 eV shifts to a lower energy, indicating that the introduction of GDY enhances the π electron excitation state. This effect may be due to interactions between GDY and Cu NPs, where electron-rich regions on the copper surface transfer electrons to GDY, filling its π* anti-bonding orbitals and leading to a higher peak intensity in G/Cu/GDY. This finding is consistent with the results from copper absorption spectra analysis. XANES analysis of the C element in G/Cu/GDY and G/Cu reveals the presence of the unique alkyne π excitation state of GDY at 286.1 eV, which is absent in the G/Cu structure, confirming the existence of GDY in the system. Additionally, in the G/Cu/GDY structure, the sp^2–C peak at 285.7 eV shifts to a lower energy, indicating that the introduction of GDY enhances the π electron excitation state. This effect may be due to interactions between GDY and Cu NPs, where electron-rich regions on the copper surface transfer electrons to GDY, filling its π* anti-bonding orbitals and leading to a higher peak intensity in G/Cu/GDY. This finding is consistent with the results from copper absorption spectra analysis.

Wavelet transform EXAFS (WT-EXAFS) contour plots (Figure 2k–o) comparing G/Cu/GDY, G/Cu, copper foil, CuO, and Cu_2O show that G/Cu/GDY and G/Cu have similar R and k values, indicating that GDY has a significant effect on the coordination environment of Cu NPs but does not change the basic configuration of the active center. Therefore, it is demonstrated that GDY successfully covers the surface of Cu NPs, and the resulting 3D structure induces hybridization of the free electrons of the copper surface with its π-electrons, making the chemical state of the copper surface closer to its oxidized state. This result is consistent with the aforementioned XPS experiments and theoretical calculations, confirming the successful construction of the 3D structured nanozyme and the formation of LEF due to electron asymmetrical distribution.

Investigation of Laccase-Like Activity of G/Cu/GDY Nanozyme

The laccase-like activity of G/Cu/GDY nanozyme was evaluated using a colorimetric reaction involving 4-aminoantipyrine (4-AP) and 2,4-dichlorophenol (2,4-DP) (Figure 3a).[43] In this assay, 2,4-DP is oxidized by laccase in the presence of O_2, which reacts with 4-AP to form a wine-red product characterized by a distinct absorption peak at 510 nm. In the absence of the nanozyme, no significant

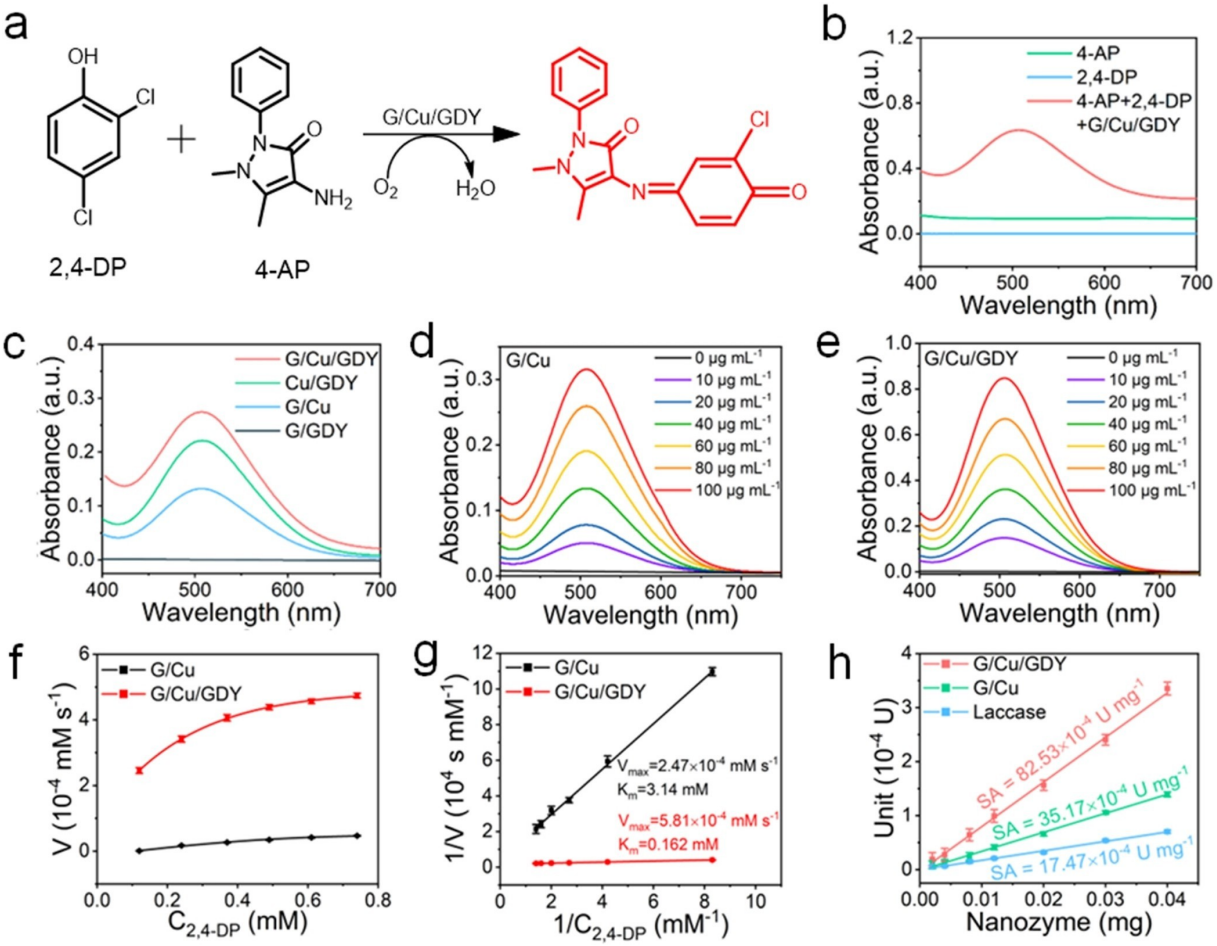

Figure 3. Laccase-like activity of G/Cu/GDY nanozyme. (a) Schematic diagram illustrating the colorimetric reaction mechanism of 2,4-dichlorophenol (2,4-DP) and 4-aminoantipyrine (4-AP). (b) UV—Vis spectra and color changes of the 4-AP, 2,4-DP, and 4-AP+ 2,4-DP +G/Cu/GDY systems. The appearance of a distinct absorption peak at 510 nm and the color change from colorless to wine-red indicate the laccase-like activity of G/Cu/GDY. (c) Comparison of laccase-like activity among different materials: G/GDY, G/Cu, Cu/GDY, and G/Cu/GDY. (d) Effect of varying concentrations of G/Cu/GDY on laccase-like activity. (e) Effect of varying concentrations of G/Cu on laccase-like activity. (f) Michaelis–Menten kinetic curves for G/Cu/GDY and G/Cu. (g) Lineweaver–Burk plots for G/Cu/GDY and G/Cu. (h) Relative activity comparison of G/Cu/GDY, G/Cu, and natural laccase. Values represent mean ± standard deviation, $n = 3$. $^{*}P < 0.05$, $^{**}P < 0.01$, $^{***}P < 0.001$.

absorption peak at 510 nm is observed when only 2,4-DP and 4-AP are present. However, upon the addition of the G/Cu/GDY nanozyme, a pronounced UV absorption peak at 510 nm is detected, and the solution changes from colorless to wine-red (Figure 3b). These results confirm the strong laccase-like activity of the G/Cu/GDY nanozyme.

The laccase-like activity of different nanozymes was compared, and the results were shown in Figure 3c. Under the same detection conditions, G/Cu/GDY showed stronger laccase-like activity. Based on this, optimization experiments of the reaction conditions were conducted, as shown in Figures S6 and S7, followed by kinetic assays based on the results obtained. The UV—Vis absorption spectra (Figure 3d, e) show the behavior of G/Cu/GDY and G/Cu at various concentrations. As the concentration increases, the solution darkens, and the intensity of the absorption peak at 510 nm rises proportionally, showing a linear relationship (Figure S8a, b). At equal concentrations, the color change and peak intensity of G/Cu/GDY are more pronounced than those of G/Cu, indicating that G/Cu/GDY exhibits higher catalytic activity. The catalytic kinetics of G/Cu/GDY, G/Cu and laccase were investigated by varying the concentration of 2,4-DP. Using Michaelis–Menten kinetics,[49] the maximum reaction rate (V_{max}) and Michaelis constant (K_m) were determined for both nanomaterials. As shown in Figure 3f, g, G/Cu/GDY demonstrated V_{max} three times higher than G/Cu and significantly lower K_m, indicating greater substrate affinity and faster reaction rates. Compared to laccase and other laccase-like nanozymes, G/Cu/GDY stands out with its lower K_m and higher V_{max} (Figure S9; Table S2),[51–56] further demonstrating its superior catalytic performance. In addition, the specific activity of G/Cu/GDY was measured as 82.53×10^{-4} Umg^{-1} (Figure 3h), significantly outperforming both natural laccase (17.47×10^{-4} Umg^{-1}) and G/Cu (35.17×10^{-4} Umg^{-1}).[43] Furthermore, the selectivity was validated through absorbance measurements with different substrates. As shown in Figure S10, G/Cu/GDY specifically

detects binary phenol derivatives, implying its excellent selectivity.

The unique physical and chemical properties of GDY not only allow effective modulation of surface electrons in Cu NPs but also provide substantial protection to these active centers. To assess the stability of Cu NPs, inductively coupled plasma mass spectrometry (ICP-MS) was performed over time on both G/Cu (Figure S11a) and G/Cu/GDY (Figure S11b). The results showed that the copper content in G/Cu/GDY remained almost unchanged, while it decreased by approximately 20 % in G/Cu. This indicates that GDY plays a key role in preventing the loss of Cu NPs, highlighting its protective function.

Ultraviolet photoelectron spectroscopy (UPS) reveals that the cutoff energy for G/Cu (4.86 eV, Figure S12a) is lower than that of G/Cu/GDY (5.38 eV, Figure S12b). The calculated work functions are 5.13 eV for G/Cu and 5.33 eV for G/Cu/GDY. In these calculations, hυ represents the excitation source (21.22 eV), E_{Fermi} is the Fermi edge, and E_{cutoff} is the measured cutoff energy.[50] These data are consistent with the work function results obtained by density functional theory (DFT) calculation (Figure S13). Using the relationship between work function and reduction potential,[50] the reduction potentials of G/Cu and G/Cu/GDY were determined to be 0.69 V and 0.89 V, respectively. As a result, covering Cu NPs with GDY lowers the reduction potential, effectively shielding the metal nanoparticles from oxidation. These findings demonstrate that GDY not only enhances laccase-like activity but also provides protective benefits to the active centers in nanozymes.

Laccase Mimetic Mechanism of G/Cu/GDY Nanozyme

To gain deeper insights into the catalytic mechanism of G/Cu/GDY nanozyme, the elementary reactions on the G/Cu/GDY surface were analyzed (Figure 4a). The formation of intermediates during the catalytic degradation of hydroquinone (HQ) by G/Cu/GDY was studied using electron paramagnetic resonance (EPR) spectroscopy. The six-line signal observed in Figure 4b, with relative intensities of 2 : 2 : 1 : 2 : 1 : 2, indicates the formation of DMPO/$O_2^{\cdot-}$ complexes, confirming the presence of $O_2^{\cdot-}$ in the system. No apparent $O_2^{\cdot-}$ signal was detected in the absence of 2,4-DP and G/Cu/GDY, suggesting that the $O_2^{\cdot-}$ signal originates from electron attachment to adsorbed O_2 during the catalytic process. This is further corroborated by the EPR spectra of hydroxyl radicals (·OH) in Figure 4c, which is generated from the hydrogenation of O_2. Moreover, a comparison with the EPR spectra of G/Cu shows that under the same conditions, G/Cu/GDY produces more ·OH and $O_2^{\cdot-}$ than G/Cu (Figure S14), indicating that G/Cu/GDY contains more unpaired electrons than G/Cu, consistent with the results shown in Figure 2d, e. Thus, G/Cu/GDY exhibits the superior laccase-like activity compared to G/Cu.

DFT calculations of the adsorption energies of O_2 on G/Cu/GDY and G/Cu (Figure 4d) reveal that GDY promotes O_2 adsorption. This is attributed to its unique sp—C π-

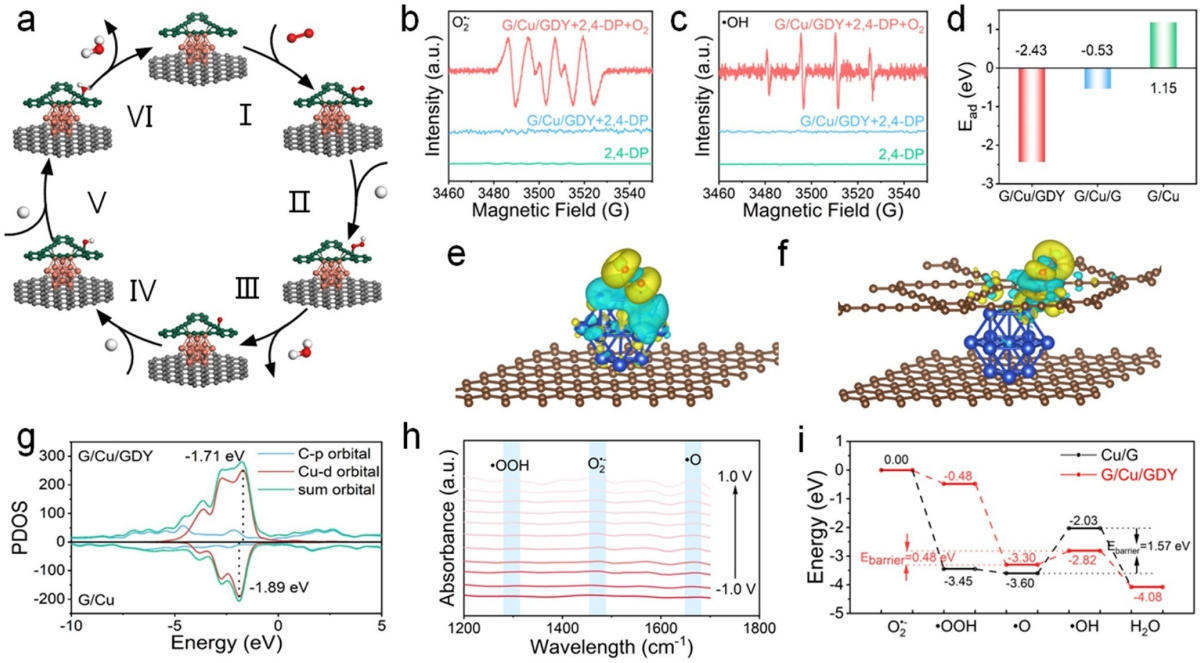

Figure 4. Laccase mimetic mechanism of G/Cu/GDY nanozyme. (a) Schematic illustration of the G/Cu/GDY nanozymes catalyzed reaction process. (b) DMPO/$O_2^{\cdot-}$ EPR spectra and (c) DMPO/·OH EPR spectra for the G/Cu/GDY system. The system containing only 2,4-DP and G/Cu/GDY was used as a control, with values reported as mean ± standard deviation, $n = 3$. (d) Comparison of the adsorption energies of oxygen on G/Cu/GDY, G/Cu/G, and G/Cu. (e) and (f) Differential charge density plots for G/Cu and G/Cu/GDY. (g) PDOS plots for G/Cu/GDY and G/Cu. (h) In situ infrared spectroscopy of G/Cu/GDY. (i) Gibbs free energy diagram of the catalytic processes of G/Cu/GDY and G/Cu nanozymes.

electron conjugation system, which interacts effectively with O_2. To elucidate how GDY enhances laccase-like activity, electron transfer during O_2 adsorption was analyzed. As shown in Figure 4e, f and Figure S15, after O_2 adsorbs onto Cu NPs, electrons predominantly localized on the distal oxygen atom, which facilitates hydrogen atom adsorption but hinders O–O bond cleavage. When GDY covers the Cu NPs, orbital hybridization occurs between GDY and Cu, resulting in increased electron transfer to the GDY surface. Upon O_2 adsorption, this hybridization with p-orbitals of O_2^{-} allows further interaction with Cu electrons, transferring them to the antibonding orbitals of O_2^{-}. This process weakens the O—O bond and promotes O_2^{-} cleavage.[32] In contrast, the electron density difference (EDD) maps after graphene coverage (Figure S16) shows no significant electron transfer, implying that this orbital hybridization is due to the unique sp–C in GDY, rather than the sp^2–C in graphene.

To further explore the interaction between Cu NPs and GDY, the projected density of states (PDOS) for G/Cu/GDY and G/Cu was calculated. As shown in Figure 4g, the d-band center of Cu in G/Cu/GDY is positioned at approximately −1.71 eV, closer to the Fermi level (E_F) than the d-band center of Cu in G/Cu at −1.89 eV. This shift suggests that Cu NPs on GDY have higher intrinsic electronic activity and better alignment of their valence and conduction bands that promotes the catalytic reaction process.[33] After oxygen adsorption, the d-band center of G/Cu/GDY shifted to −1.87 eV (Figure S17), which is less negative compared to the shift observed for G/Cu, ranged from −1.89 eV to −1.96 eV, indicating that the copper atoms in G/Cu/GDY lose more electrons to the oxygen molecules during adsorption compared to those in G/Cu. The greater downward shift in the d-band center for G/Cu/GDY suggests that this material is more favorable for O_2 adsorption and activation.[33] The electric field generated by the interaction between GDY and Cu NPs alters the electronic structure of the surface copper atoms, which affects O_2 adsorbs and desorbs, highlighting the strong electronic interaction between the substrate and the catalytic center. Consequently, it is concluded that this interaction influences the ability of G/Cu/GDY to activate O_2.

In situ infrared spectroscopy further demonstrates the generation of radical species during the catalytic reaction. Significant changes in peak intensities were observed as the applied voltage increased (Figure 4h). Specifically, stretching vibration peaks for ·OOH was detected at 1294 cm^{-1}, respectively, with a marked increase in absorption intensity as the voltage rose, validating the occurrence of catalytic reactions. Additionally, the characteristic peak at 1684 cm^{-1}, attributed to the C=O stretching vibration of O_2 adsorbed on the GDY surface,[28] shows the most pronounced change with increasing voltage, highlighting the key role of O–O bond cleavage in the reaction. The vibration peak positions of $*O_2$, *OOH, and *O from the density functional perturbation theory (DFPT) calculations closely align with those observed in in situ infrared spectra (Figure S18), validating the accuracy of the computational model and parameter settings. This agreement further supports the ability of the model to accurately represent the radicals generated during the reaction.

Gibbs free energy changes were calculated for different reaction stages, with model structure optimizations and free energy variations shown in Figure 4i and Figures S19, S20. In the initial step of the reaction, the surface intermediate energy decreases for both G/Cu and G/Cu/GDY, with a larger reduction observed for G/Cu/GDY at −3.44 eV, indicating that after loading GDY, the nanozyme more effectively adsorbs and activates O_2, promoting hydrogen extraction from binary phenol to form the OOH intermediate. Following this, the O–O bond breaks and dissociates, producing water molecules and an O* species from binary phenol. During this process, the energy continues to decrease in both models, with no significant energy barrier. In the third reaction step of the reaction, hydrogen atoms from hydroquinone are extracted by the O* species on the surfaces of both G/Cu/GDY and G/Cu, resulting in the formation of ·OH. This step involves overcoming an energy barrier, making it the rate-determining step. Notably, the energy barrier for G/Cu/GDY is 0.48 eV, which is considerably lower than that for G/Cu at 1.57 eV, demonstrating that G/Cu/GDY can more effectively activate binary phenol and exhibit higher laccase-like activity compared to G/Cu.

Electrochemical Applications of G/Cu/GDY Nanozyme

The high laccase-like activity and exceptional stability of G/Cu/GDY nanozyme make it a promising candidate for the rapid electrochemical detection of binary phenol derivatives. To evaluate the performance of various modified electrodes, cyclic voltammetry (CV) was conducted. As depicted in Figure 5a, G/Cu exhibits the highest redox peak currents and lower redox potentials, which is attributed to the high electron transfer efficiency of the thin-layer graphene. When modified with G/Cu/GDY nanozyme, the redox currents increase significantly compared to Cu/GDY and G/Cu, along with a further reduction in redox potential. This suggests that the strong interaction between GDY and Cu NPs promotes efficient electron transfer at the electrode surface, thereby improving electrochemical activity. In addition, the electrochemical surface area of G/Cu/GDY was calculated by analyzing CV curves at various scan rates (Figure 5b). In comparison, the surface areas of glassy carbon electrode (GCE), G/Cu, and Cu/GDY were evaluated under same conditions (Figure S21). The electrochemically active surface areas for the bare electrode, G/Cu, Cu/GDY, and G/Cu/GDY are 0.094, 0.287, 0.131, and 0.209 cm^2, respectively, demonstrating that the ultrathin GDY/G structure provides both a high peak current and a large electrochemical active surface area. The effect of scan rate on the redox peak current of hydroquinone was also investigated using CV. The redox peak current increased linearly with the square root of the scan rate (Figure 5c), indicating that the electrochemical oxidation and reduction of hydroquinone at the modified electrode are diffusion-controlled processes. Furthermore, impedance plots (Figure 5d) for different materials confirm that the presence of

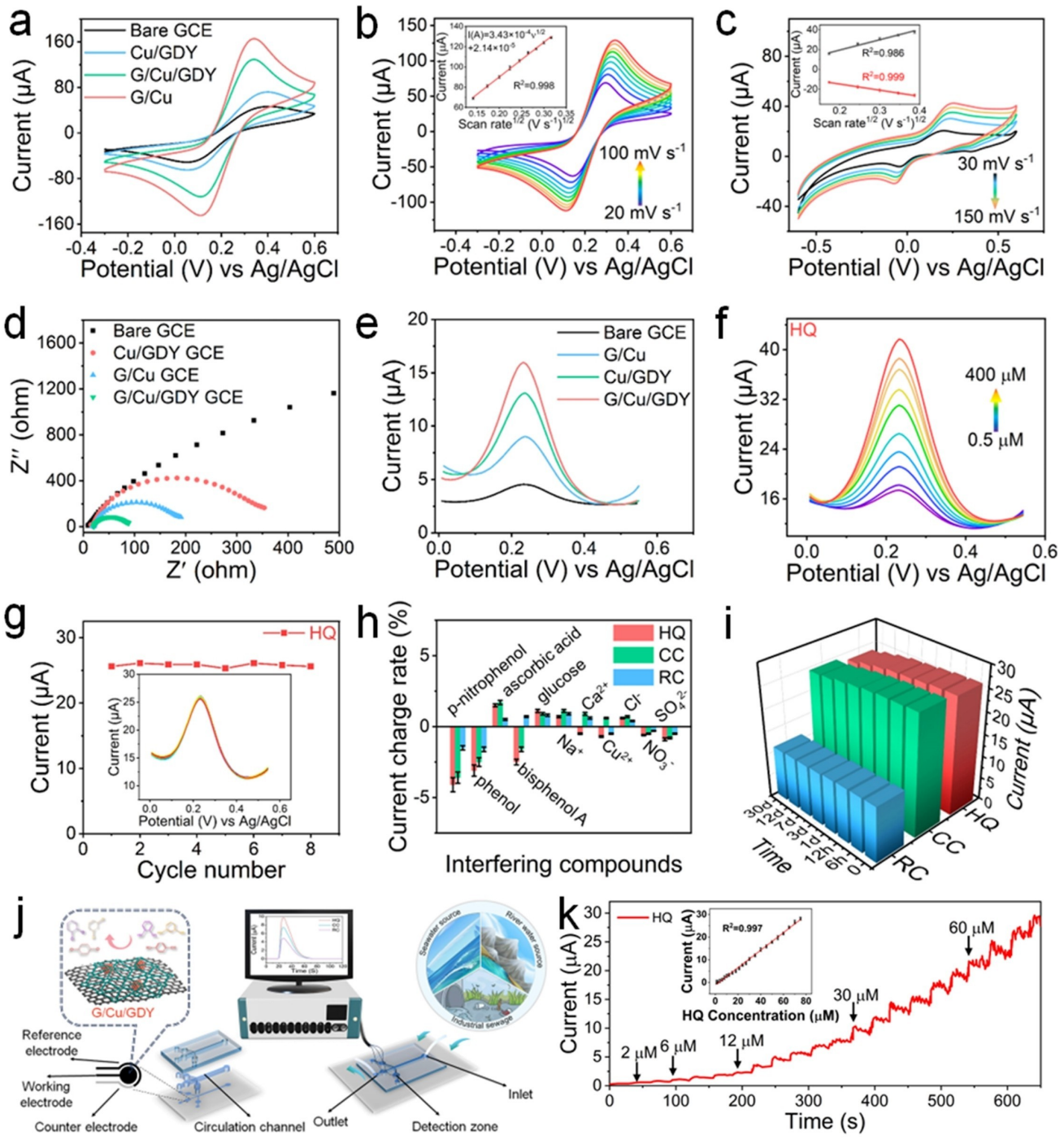

Figure 5. Electrochemical detection of hydroquinone. (a) Cyclic voltammetry (CV) curves of bare GCE, Cu/GDY, G/Cu/GDY, and G/Cu in 5.0 mM $[Fe(CN)_6]^{3-}/[Fe(CN)_6]^{4-}$ solution containing 0.1 M KCl. (b) CV cyclic curves of G/Cu/GDY at scan rates ranging from 20 to 100 mVs^{-1}. (c) Impedance plots for different materials. (d) Differential pulse voltammetry (DPV) curves for the detection of 20 μM hydroquinone on various modified electrodes in pH 7 PBS buffer. (e) CV curves of the G/Cu/GDY modified electrode in pH 7 PBS buffer containing 20 μM hydroquinone at different scan rates, with the inset showing the linear relationship between the redox peak current and the square root of the scan rate. (f) DPV curves for hydroquinone detection using the G/Cu/GDY modified electrode. (g) Reproducibility of hydroquinone detection with the G/Cu/GDY modified electrode. (h) Selectivity of G/Cu/GDY for hydroquinone, catechol and resorcinol. detection. (i) Stability of G/Cu/GDY. (j) Schematic diagram of practical application detection. (k) Real-time I–t curve for hydroquinone detection. Values represent mean ± standard deviation, $n = 3$. $^{*}P < 0.05$, $^{**}P < 0.01$, $^{***}P < 0.001$.

GDY significantly enhances the electrochemical performance of Cu NPs.

Differential pulse voltammetry (DPV) was employed to evaluate the performance of various modified electrodes in

detecting hydroquinone. As shown in Figure 5e, the bare GCE electrode produces the lowest oxidation current. In contrast, the Cu/GDY and G/Cu modified electrodes show significantly higher oxidation currents, with the G/Cu/GDY electrode exhibiting the highest peak, consistent with the CV results. Remarkably, the Cu/GDY electrode outperforms G/Cu due to the ultrathin GDY layer, which provides more anchoring sites for Cu atoms, increasing active sites and enhancing laccase-like activity. Furthermore, the π–π interactions between GDY and hydroquinone facilitate the capture of hydroquinone molecules, demonstrating that GDY not only protects Cu NPs and improves their catalytic activity but also enhances the capture of target substances. The electrochemical behavior of G/Cu/GDY was optimized by adjusting pH levels and drop volumes using DPV. The response current increases as the pH rises from 4.0 to 6.0, peaking at pH 6.0 before decreasing at higher pH values (Figure S22a), which aligns with optimal laccase-like activity in colorimetric assays. The effect of nanozyme quantity was tested by varying the drop volume of the G/Cu/GDY dispersion (Figure S22b). The response current peaks at 5 μL, with further additions leading to a slight decrease, indicating an optimal amount for maximizing performance.

Given the strong electrochemical response of G/Cu/GDY, DPV was used to detect varying concentrations of hydroquinone (HQ), resorcinol (RC), and catechol (CC). As shown in Figure 5f and Figure S23, the current signals for hydroquinone, resorcinol, and catechol increase with concentration, confirming effective detection capabilities. The limit of detection (LOD) was determined based on the correlation between peak current changes and analyte concentration. For catechol, the LOD was 0.52 μM (Figure S24a), while catechol and resorcinol had LODs of 0.16 μM and 0.23 μM (Figure S24b, c), respectively. These LODs and linear ranges compare favorably with previously reported electrodes (Table S3).[57–61] The enhanced sensitivity and broader detection range enable precise concentration measurements in complex environments, ensuring reliable and effective monitoring for applications such as low-concentration polluted water and water quality assessments.

The reproducibility of the G/Cu/GDY modified electrode was examined across eight experiments, yielding relative standard deviations (RSDs) of 1.05% for hydroquinone, 1.29% for resorcinol, and 0.89% for catechol, respectively (Figure 5g; Figure S25). These results highlight the excellent reproducibility, stability, and selectivity. As shown in Figure 5h, interference from potential contaminants is minimal, with phenol and other substances causing less than 5% interference, while common biological substances and ions cause less than 3%, confirming the high selectivity of the G/Cu/GDY electrode. Long-term stability was demonstrated through 30-day continuous detection, where the electrode retained over 89% of its initial response for hydroquinone, resorcinol, and catechol (Figure 5i), and no obvious change in the nanozyme (Figure S26). The stability is due to the robust physical and chemical properties of GDY and graphene, making the G/Cu/GDY nanozyme reliable for extended use.

To address the need for efficiency and precision, a microfluidic chip-based electrochemical detection device was designed (Figure 5j). This device integrates signal transmission, analysis, and wireless communication, and can detect HQ, RC, and CC simultaneously. Noticeably, G/Cu/GDY was photolithographically printed onto conductive glass, enabling real-time sensing with excellent electrochemical response and stability. The detection process involves filtering water to remove large particles before pumping it into the sensing device for analysis, and then recycling the solution (Figure S27). As shown in Figure 5k, significant real-time current changes occur when detecting phenolic substances.

The practical application of the G/Cu/GDY modified electrode was evaluated by testing it with tap water and river water samples spiked with different concentrations of hydroquinone, resorcinol, and catechol. Table S4 shows that the detection rates range from 95.08 % to 104.9 %, with RSDs between 1.47 % and 4.43 %, indicating high reliability and consistency in real sample analysis, thereby demonstrating the potential of the G/Cu/GDY electrode in water quality monitoring.

Microplastic Degradation by G/Cu/GDY Nanozyme

The G/Cu/GDY nanozyme was tested for its effectiveness in degrading low-density polyethylene (LDPE) microplastics. The degradation efficiency was assessed using LDPE powders. While natural laccase is capable of degrading LDPE (Figure 6a, b), its performance declines significantly at higher temperatures due to enzyme denaturation. In contrast, the G/Cu/GDY nanozyme shows superior degradation under the same conditions, attributed to its enhanced O_2 activation and the thermal stability of its copper active centers. In-depth analysis of weight loss in degradation products at different pH levels (Figure S28) reveals that the optimal degradation occurs at pH 6. In addition, total organic carbon (TOC) measurement confirms that the G/Cu/GDY nanozyme could break down LDPE into water soluble carbon containing compounds (Figure 6c), with TOC levels rising significantly over time.

The mechanism of G/Cu/GDY catalyzed degradation of LDPE was further investigated by various techniques under optimum conditions. The change in molecular weight of LDPE before and after the reaction was shown by permeation gel chromatography (GPC). As shown in Figure 6d, the molecular weight of LDPE significantly decreases after 20 h, indicating that G/Cu/GDY effectively breaks down high molecular weight LDPE into smaller fragments. The functional groups produced and the changes occurring in the degradation of LDPE by G/Cu/GDY were demonstrated by Fourier transform infrared (FT-IR) spectroscopy. A O–H stretching vibration at 3380 cm^{-1} indicates that G/Cu/GDY promotes the generation of reactive oxygen species, leading to the cleavage of polyethylene chains and the formation of oxygen-containing functional groups (Figure 6e). The reduction of C–H bond peaks at 2890 cm^{-1} and 2950 cm^{-1} confirms the formation of terminal oxygen groups, under-

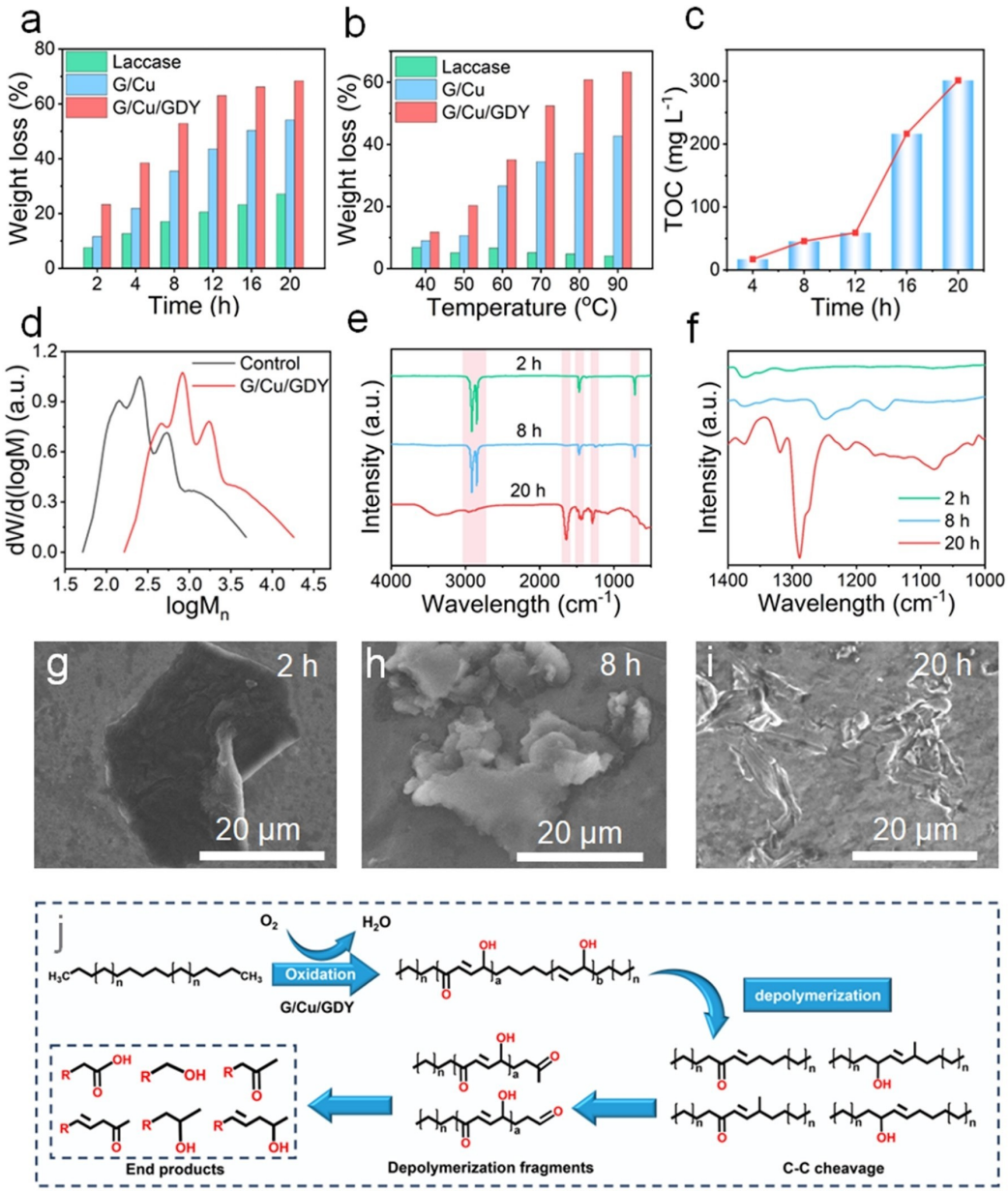

Figure 6. Catalytic degradation of microplastics by G/Cu/GDY. Degradation of polyethylene by G/Cu/GDY, G/Cu, and natural laccase under (a) different reaction times and (b) various temperatures and conditions. (c) Total organic carbon (TOC) values in the residual solution at different reaction times. The experiment was repeated three times and the optimal results were taken and displayed in the Figure. (d) Gel permeation chromatography (GPC) of polyethylene degradation. (e) Fourier transform infrared (FT-IR) spectra of products after polyethylene degradation at 90 °C, pH 6, 20 h. (f) Magnified FTIR spectra. (g–i) SEM images of microplastics after reaction times of (g) 2 h, (h) 8 h, and (i) 20 h. (j) Roadmap of the LDPE degradation catalyzed by G/Cu/GDY.

scoring the critical role of G/Cu/GDY in the degradation process. Figure 6f reveals shifts at 1290 cm^{-1} and 1650 cm^{-1}, corresponding to the stretching vibrations of C–O and C=O bonds, respectively. Additionally, SEM images provide visual evidence of LDPE degradation over time (Figure 6g–i). The polyethylene structure progressively disintegrated from an intact sheet to fragments, and eventually to fine filaments after 20 h, demonstrating the effective breakdown of microplastics by G/Cu/GDY. The proposed degradation pathway (Figure 6j) begins with the oxidation of LDPE by G/Cu/GDY, incorporating oxygen-containing groups such as ketones and forming olefinic bonds. This is followed by the cleavage of C–C bonds at these sites, further oxidation at the terminal groups, and the formation of depolymerized fragments containing carboxyl and hydroxyl groups. The process ultimately yields low molecular weight acids and alcohols, confirming that G/Cu/GDY can break down polyethylene into environmentally benign substances, highlighting its potential for environmental protection.

Conclusions

In summary, this study presents a simple method for biomimetically constructing the 3D geometric and electronic structure in the nanozyme. This approach addresses the challenges faced by conventional 3D structure nanozymes, which have been limited by the complexity of SAzymes and difficult fabrication processes. Theoretical calculations and in situ experiments confirm that GDY facilitates the modulation of surface electrons on Cu NPs through orbital hybridization between sp-C and Cu d-orbitals, which plays a crucial role in coordinating the electronic distribution between Cu NPs and O_2 during substrate decomposition, enhancing electron transfer to the anti-bonding orbitals of O_2. This promotes the cleavage of the O—O bond and the desorption of H_2O, significantly increasing laccase-like activity to 82.53 Umg^{-1}, which is 4.72 times higher than that of natural laccase, demonstrating its wide applicability in pollutant detection and degradation. Additionally, the G/Cu/GDY nanozyme exhibited high sensitivity, excellent selectivity, and recyclability in detecting phenolic compounds, as well as efficiently degrading microplastics. Overall, this study provides a universal method for achieving the 3D structure of nanozymes through the hybridization of large d-π orbitals, offering valuable insights for the rational design of nanozymes.

Supporting Information

The authors have cited additional references within the Supporting Information.

Acknowledgements

This work was supported by the National Natural Science Foundation of China (Grant No. 22279067, 32371465), Taishan Scholar Talent Program (tsqn202408198), and Natural Science Foundation of Shandong Province (Grant No. ZR2021MB111, ZR2020MB026, ZR2023ME076).

Conflict of Interest

The authors declare no competing financial interest.

Data Availability Statement

The data that support the findings of this study are available in the supplementary material of this article.

Keywords: biomimetic · d-π orbital hybridization · graphdiyne · local electric field · nanozyme · three-dimensional structure

[1] W. Yang, X. Yang, L. Zhu, H. Chu, X. Li, W. Xu, *Coord. Chem. Rev.* **2021**, *448*, 214170.
[2] H. Wei, E. Wang, *Chem. Soc. Rev.* **2013**, *42*, 6060.
[3] J. Wu, X. Wang, Q. Wang, Z. Lou, S. Li, Y. Zhu, L. Qin, H. Wei, *Chem. Soc. Rev.* **2019**, *48*, 1004.
[4] A. Das, S. Ghosh, A. Mishra, A. Som, V. B. Banakar, S. S. Agasti, S. J. George, *J. Am. Chem. Soc.* **2024**, *146*, 14844.
[5] J.-L. Chen, X. Wang, F. Yang, C. Cao, G. Otting, X.-C. Su, *Angew. Chem. Int. Ed.* **2016**, *55*, 13744.
[6] G. Y. Tonga, Y. Jeong, B. Duncan, T. Mizuhara, R. Mout, R. Das, S. T. Kim, Y.-C. Yeh, B. Yan, S. Hou, V. M. Rotello, *Nat. Chem.* **2015**, *7*, 597.
[7] X. Li, X. Wu, Y. Zhao, Y. Lin, J. Zhao, C. Wu, H. Liu, L. Shan, L. Yang, L. Song, J. Jiang, *Adv. Mater.* **2023**, *35*, 2302467.
[8] H.-C. Zhang, P.-X. Cui, D.-H. Xie, Y.-J. Wang, P. Wang, G.-P. Sheng, *Adv. Sci.* **2023**, *10*, 2205681.
[9] G. Li, H. Liu, T. Hu, F. Pu, J. Ren, X. Qu, *J. Am. Chem. Soc.* **2023**, *145*, 16835.
[10] Q. Zhao, M. Zhang, Y. Gao, H. Dong, L. Zheng, Y. Zhang, J. Ouyang, N. Na, *J. Am. Chem. Soc.* **2024**, *146*, 14875.
[11] Y. Wang, V. K. Paidi, W. Wang, Y. Wang, G. Jia, T. Yan, X. Cui, S. Cai, J. Zhao, K.-S. Lee, L. Y. S. Lee, K.-Y. Wong, *Nat. Commun.* **2024**, *15*, 2239.
[12] S. Gao, H. Lin, H. Zhang, H. Yao, Y. Chen, J. Shi, *Adv. Sci.* **2019**, *6*, 1801733.
[13] L. Zhang, N. Jin, Y. Yang, X.-Y. Miao, H. Wang, J. Luo, L. Han, *Nano-Micro Lett.* **2023**, *15*, 228.
[14] R. Tian, H. Ma, W. Ye, Y. Li, S. Wang, Z. Zhang, S. Liu, M. Zang, J. Hou, J. Xu, Q. Luo, H. Sun, F. Bai, Y. Yang, J. Liu, *Adv. Funct. Mater.* **2022**, *32*, 2204025.
[15] S. Liang, X.-L. Wu, J. Xiong, X. Yuan, S.-L. Liu, M.-H. Zong, W.-Y. Lou, *Chem. Eng. J.* **2022**, *450*, 138220.
[16] T. Xie, Z. Liu, G. Wang, *Nat. Plants* **2020**, *6*, 231.
[17] A. J. Augustine, C. Kjaergaard, M. Qayyum, L. Ziegler, D. J. Kosman, K. O. Hodgson, B. Hedman, E. I. Solomon, *J. Am. Chem. Soc.* **2010**, *132*, 6057.
[18] H. Zhang, P. Wang, J. Zhang, Q. Sun, Q. He, X. He, H. Chen, H. Ji, *Angew. Chem. Int. Ed.* **2024**, *63*, e202316779.
[19] Z. Li, B. Ding, J. Li, H. Chen, J. Zhang, J. Tan, X. Ma, D. Han, P. a. Ma, J. Lin, *Angew. Chem. Int. Ed.* **2024**, e202413661. DOI: 10.1002/anie.202413661.
[20] R. Zeng, Q. Gao, L. Xiao, W. Wang, Y. Gu, H. Huang, Y. Tan, D. Tang, S. Guo, *J. Am. Chem. Soc.* **2024**, *146*, 10023.
[21] P. B. O'Mara, P. Wilde, T. M. Benedetti, C. Andronescu, S. Cheong, J. J. Gooding, R. D. Tilley, W. Schuhmann, *J. Am. Chem. Soc.* **2019**, *141*, 14093.
[22] M. Pan, J. Li, X. Zhang, S. Liu, J. W. Chew, B. Pan, *J. Mater. Chem. A* **2023**, *11*, 5095.
[23] H. Zhang, L. Huang, J. Chen, L. Liu, X. Zhu, W. Wu, S. Dong, *Nano Energy* **2021**, *83*, 105798.
[24] K.-H. Wu, Y. Liu, X. Tan, Y. Liu, Y. Lin, X. Huang, Y. Ding, B.-J. Su, B. Zhang, J.-M. Chen, W. Yan, S. C. Smith, I. R. Gentle, S. Zhao, *Chem Catal.* **2022**, *2*, 372.
[25] C. Ye, J. Shan, C. Zhu, W. Xu, L. Song, Y. Zhu, Y. Zheng, S.-Z. Qiao, *Adv. Energy Mater.* **2023**, *13*, 2302190.
[26] Y. Ouyang, Y. Biniuri, M. Fadeev, P. Zhang, R. Carmieli, M. Vázquez-González, I. Willner, *J. Am. Chem. Soc.* **2021**, *143*, 11510.
[27] L. Li, S. Huang, R. Cao, K. Yuan, C. Lu, B. Huang, X. Tang, T. Hu, X. Zhuang, Y. Chen, *Small* **2022**, *18*, 2105387.
[28] Z. Zheng, L. Qi, X. Luan, S. Zhao, Y. Xue, Y. Li, *Nat. Commun.* **2024**, *15*, 7331.
[29] W. Feng, Y. Jiang, F. Ge, Q. Bai, J. Yang, L. Shang, R. Cao, G. Niu, L. Wang, Z. Zhu, N. Sui, *Appl. Catal. B-Environ.* **2024**, *349*, 123868.
[30] X. Sun, M. Duan, R. Li, Y. Meng, Q. Bai, L. Wang, M. Liu, Z. Yang, Z. Zhu, N. Sui, *Anal. Chem.* **2022**, *94*, 13598.
[31] Q. Bai, K. Xiong, C. Zhang, L. Wang, W. Han, Q. Zhu, F. Du, W. W. Yu, N. Sui, *J. Colloid Interface Sci.* **2023**, *646*, 802.

[32] C. Pan, C. Wang, X. Zhao, P. Xu, F. Mao, J. Yang, Y. Zhu, R. Yu, S. Xiao, Y. Fang, H. Deng, Z. Luo, J. Wu, J. Li, S. Liu, S. Xiao, L. Zhang, Y. Guo, *J. Am. Chem. Soc.* **2022**, *144*, 4942.
[33] J. Yu, W. Chen, F. He, W. Song, C. Cao, *J. Am. Chem. Soc.* **2023**, *145*, 1803.
[34] S. Liu, Q. Bai, Y. Jiang, Y. Gao, Z. Chen, L. Shang, S. Zhang, L. Yu, D. Yang, N. Sui, Z. Zhu, *Small* **2024**, *20*, 2308403.
[35] L. Hui, D. Yan, X. Zhang, H. Wu, J. Li, Y. Li, *Angew. Chem. Int. Ed.* **2024**, *63*, e202410413.
[36] Y. Wu, Y. Xie, Z. Jin, *Appl. Catal. B* **2024**, *357*, 124348.
[37] J. Liao, L. Zhang, B. Sun, D. Wang, Z. Zhang, W. Ma, Z. Wang, Y. Wang, Q. Wang, W. Yin, Z. Gu, *Nano Today* **2024**, *55*, 102204.
[38] Y. Gao, Y. Xue, S. Chen, Y. Zheng, S. Chen, X. Zheng, F. He, C. Huang, Y. Li, *Angew. Chem. Int. Ed.* **2024**, *63*, e202406043.
[39] S. Zhan, X. Chen, B. Xu, L. Wang, L. Tong, R. Yu, N. Yang, D. Wang, *Nano Today* **2022**, *47*, 101626.
[40] J. Li, Y. Yi, X. Zuo, B. Hu, Z. Xiao, R. Lian, Y. Kong, L. Tong, R. Shao, J. Sun, J. Zhang, *ACS Nano* **2022**, *16*, 3163.
[41] Y. Sun, X. Wang, H. Zhang, X. Gao, X. Wang, S. Wang, Z. Tang, S. Li, K. Nie, J. Xie, Z. Yang, Y.-M. Yan, *ACS Catal.* **2024**, *14*, 1351.
[42] T. Gan, J. Yang, D. Morris, X. Chu, P. Zhang, W. Zhang, Y. Zou, W. Yan, S.-H. Wei, G. Liu, *Nat. Commun.* **2021**, *12*, 2741.
[43] M. Chen, H. Zhang, L. Tian, H. Lv, C. Chen, X. Liu, W. Wang, Y. Wang, Y. Zhao, J. Wang, H. Zhou, Y. Mao, C. Xiong, Y. Wu, *ACS Appl. Mater. Interfaces* **2023**, *15*, 407.
[44] Y. Xia, L. Xia, X. Lin, *Adv. Sci.* **2023**, *10*, 2300210.
[45] J.-X. Wang, A. C. Vilbert, C. Cui, E. N. Mirts, L. H. Williams, W. Kim, Y. Jessie Zhang, Y. Lu, *Angew. Chem. Int. Ed.* **2023**, *62*, e202314019.
[46] H. Gu, L. Zhong, G. Shi, J. Li, K. Yu, J. Li, S. Zhang, C. Zhu, S. Chen, C. Yang, Y. Kong, C. Chen, S. Li, J. Zhang, L. Zhang, *J. Am. Chem. Soc.* **2021**, *143*, 8679.
[47] Y. Yi, J. Li, Z. Gao, W. Liu, Y. Zhao, M. Wang, W. Zhao, Y. Han, J. Sun, J. Zhang, *Adv. Mater.* **2022**, *34*, 2202685.
[48] G. Yang, J. Zhu, P. Yuan, Y. Hu, G. Qu, B.-A. Lu, X. Xue, H. Yin, W. Cheng, J. Cheng, W. Xu, J. Li, J. Hu, S. Mu, J.-N. Zhang, *Nat. Commun.* **2021**, *12*, 1734.
[49] B. Jiang, D. Duan, L. Gao, M. Zhou, K. Fan, Y. Tang, J. Xi, Y. Bi, Z. Tong, G. F. Gao, N. Xie, A. Tang, G. Nie, M. Liang, X. Yan, *Nat. Protoc.* **2018**, *13*, 1506.
[50] H. Qi, P. Yu, Y. Wang, G. Han, H. Liu, Y. Yi, Y. Li, L. Mao, *J. Am. Chem. Soc.* **2015**, *137*, 5260.
[51] Y. Lei, B. He, S. Huang, X. Chen, J. Sun, *Molecules* **2022**, *27*, 4712.
[52] J. Wang, R. Huang, W. Qi, R. Su, Z. He, *J. Hazard. Mater.* **2022**, *429*, 128404.
[53] M. Li, Y. Xie, R. Li, N. Li, X. Su, *Biosens. Bioelectron.* **2024**, *261*, 116501.
[54] J. Wang, R. Huang, W. Qi, R. Su, Z. He, *Chem. Eng. J.* **2022**, *434*, 134677.
[55] T.-Q. Chai, J.-L. Wang, G.-Y. Chen, L.-X. Chen, F.-Q. Yang, *Sensors* **2023**, *23*, 8137.
[56] J. Wang, R. Huang, W. Qi, R. Su, B. P. Binks, Z. He, *App. Catal. B-environ.* **2019**, *254*, 452.
[57] D. Yin, J. Liu, X. Bo, L. Guo, *Anal. Chim. Acta* **2020**, *1093*, 35.
[58] H. Yin, Q. Zhang, Y. Zhou, Q. Ma, T. liu, L. Zhu, S. Ai, *Electrochim. Acta* **2011**, *56*, 2748.
[59] Y. Chen, X. Liu, S. Zhang, L. Yang, M. Liu, Y. Zhang, S. Yao, *Electrochim. Acta* **2017**, *231*, 677.
[60] H. Zhang, X. Bo, L. Guo, *Sensor. Actuat. B-Chem.* **2015**, *220*, 919.
[61] T. Yang, Y. Li, G. Liu, J. Tong, P. Zhang, B. Feng, K. Tian, X. Liu, T. Qing, *J. Hazard. Mater.* **2024**, *477*, 135292.

Manuscript received: September 28, 2024
Accepted manuscript online: December 23, 2024
Version of record online: January 7, 2025